Vacuum 86 (2012) 1505–1512

Contents lists available at SciVerse ScienceDirect

Vacuum

journal homepage: www.elsevier.com/locate/vacuum

Oxidation behavior of Ti–B–C–N coatings deposited by reactive magnetron sputtering

Xiangyang Chen [a], Shengli Ma [a,*], Kewei Xu [a], Paul K. Chu [b]

[a] State-Key Laboratory for Mechanical Behavior of Materials, Xi'an Jiaotong University, Shan'xi Province, Xi'an 710049, China
[b] Department of Physics and Materials Science, City University of Hong Kong, Tat Chee Avenue, Kowloon, Hong Kong, China

ARTICLE INFO

Article history:
Received 8 October 2011
Received in revised form
21 February 2012
Accepted 2 March 2012

Keywords:
Reactive magnetron sputtering
Ti–B–C–N coatings
Oxidation behavior

ABSTRACT

Quaternary Ti–B–C–N coatings with different carbon concentrations are deposited on high-speed steel substrates by reactive magnetron sputtering. The oxidation behavior between 300 and 800 °C under ambient conditions is studied by scanning electron microscopy, high-resolution transmission electron microscopy, Vickers micro-hardness, and X-ray diffraction. The Ti–B–C–N coatings with smaller carbon contents have better oxidation resistance and the oxidation process can be divided into two stages: low-speed oxidation below 700 °C and high-speed oxidation above 700 °C. An oxidation mechanism is proposed to explain the relationship between the reaction with oxygen and observed oxidation behavior.

1. Introduction

Ti–B–N, a TiN-based coating that offers good wear resistance, high hardness, and good oxidation resistance at elevated temperature is used by the cutting tool industry [1–5],.However, tribological studies show that the friction coefficient of typical Ti–B–N coatings against steel balls in air is about 0.6 which may be too high for some applications [6–8]. Hence, carbon which offers self-lubricating effects has been incorporated into Ti–B–N coatings to form quaternary Ti–B–C–N coatings in order to reduce the friction coefficient. Ti–B–C–N coatings have been prepared by different deposition techniques such as chemical vapor deposition (CVD) [9], plasma-enhanced CVD [10,11], and reactive magnetron sputtering (RMS) [12,13]. The mechanical and tribological properties studied by Zhong D on Ti–B–C–N thin films deposited by magnetron sputtering in different argon-nitrogen atmospheres shows that the Ti–B–C–N film with 10% nitrogen exhibited the best adhesion to substrate, lowest residual stress, and best tribological performance [12]. The corresponded oxidation resistance shows that nitrogen addition leads to the oxidation rates of the coatings increase, and the oxidation process of the Ti–B–C–N coatings is mainly diffusion-controlled [14]. Vyas A and our previous studies on Ti–B–C–N coatings show that addition appropriate amount of carbon to the coatings is favorable for the hardness value enhancement, and carbon content increase can decrease the friction coefficient to a minimum value of about 0.2, the volume wear rates of coatings also decrease as carbon content increase, which indicates that carbon addition is an effect method for improving the tribological properties of Ti–B–C–N coatings [15,16]. However, the carbon content effect on the oxidation behavior of Ti–B–C–N coatings at elevated temperature and the related mechanism are not well understood thereby hampering wider acceptance by the industry. In the work reported here, Ti–B–C–N coatings with different carbon concentrations are deposited by reactive magnetron sputtering and the oxidation behavior between 300 and 800 °C is studied.

2. Experimental details

The quaternary Ti–B–C–N coatings were deposited on high-speed steel (W18Cr4V) substrates by reactive magnetron sputtering (RMS). Three pairs of dual-magnetron targets including two sintered titanium targets, two sintered graphite targets, and two sintered B_4C targets were fixed on two sides of the chamber. High-purity argon (99.999%) was used as the sputtering gas and high-purity nitrogen (99.999%) was used as the reactive gas to deposit the Ti–B–C–N coatings. Prior to deposition, the substrates (Φ24 mm × 9 mm) were mechanically polished, cleaned ultrasonically with acetone for 30 min, washed in deionized water, and dried under nitrogen atmosphere. The vacuum chamber was first evacuated to a base pressure of 3.5×10^{-3} Pa and then Ar plasma sputtering was conducted to clean the substrates for 30 min at a bias voltage of −1000 V before actual deposition. The deposition

* Corresponding author.
E-mail address: slma@mail.xjtu.edu.cn (S. Ma).

0042-207X/$ – see front matter © 2012 Elsevier Ltd. All rights reserved.
doi:10.1016/j.vacuum.2012.03.001

Table 1
Composition of the as-deposited Ti–B–C–N coatings.

Sample No.	C target power (kW)	Ti (at.%)	B (at.%)	C (at.%)	N (at.%)	O (at.%)
1	0	26.8	18.5	28.9	25.1	0.7
2	3	22.1	13.5	48.8	14.8	0.8
3	4	16.9	13.1	54.2	14.6	1.2

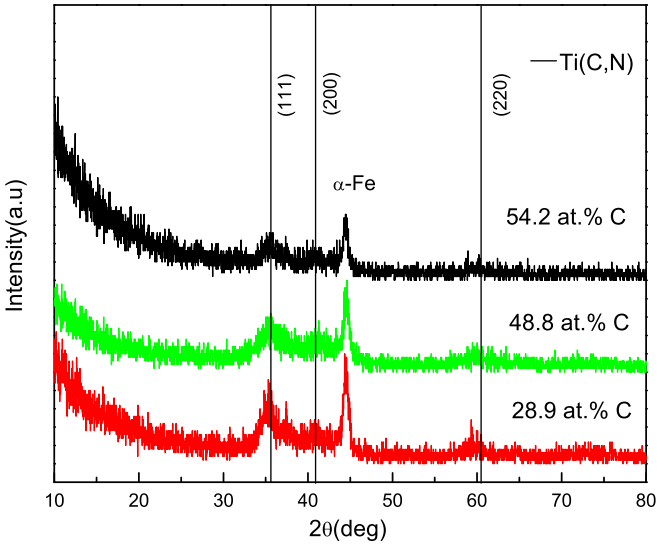

Fig. 1. X-ray diffraction patterns of the as-deposited Ti–B–C–N coatings with different carbon contents.

pressure, bias voltage, substrate temperature, nitrogen flow rate, Ti target power, and B_4C target power were at 3×10^{-1} Pa, −100 V, 150 °C, 2 sccm, 2 kW and 1 kW, respectively. The carbon concentrations in the Ti–B–C–N coatings were varied by changing the power applied to the graphite target from 0 kW to 3 kW and 4 kW.

Annealing was performed in the SRJXZ-9 resistor furnace in the temperature range of 300–800 °C in air for 1 h. The carbon content, composition, and chemical states were determined by X-ray photoelectron spectrometry (XPS, PHI 5802) with a monochromatized Al K_α source after sputter-cleaning with Ar ions for 5 min. The micro-structure of the coatings was characterized by high-resolution transmission electron microscopy (HR-TEM, JEM 2100F) and X-ray diffraction (XRD, D/max-3C), the average crystallite size of the nano-crystalline was calculated from broadening of the main peaks using the Scherrer equation [17], the lattice parameter of Ti(C, N) solid solution is calculated by the following equation:

$$a = d_{hkl} \times \sqrt{h^2 + k^2 + l^2}$$

Where a is the lattice parameter (nm), d_{hkl} is the interplanar crystal spacing of {hkl} family of crystal planes (nm), and h, k, and l is indices of crystal face. The surface roughness was determined on a TALYSURF-4 mechanical profilometer and the variation in the surface morphology with annealing temperature was monitored by FE-SEM (JSM-7000F), the cross-sectional depth composition profiles of coatings were detected by energy dispersive X-ray spectroscopy (EDX) attach to FE-SEM. The micro-hardness was determined using an MH-5 indentation tester equipped with a Vickers diamond indenter using a load of 25 g. The load was kept

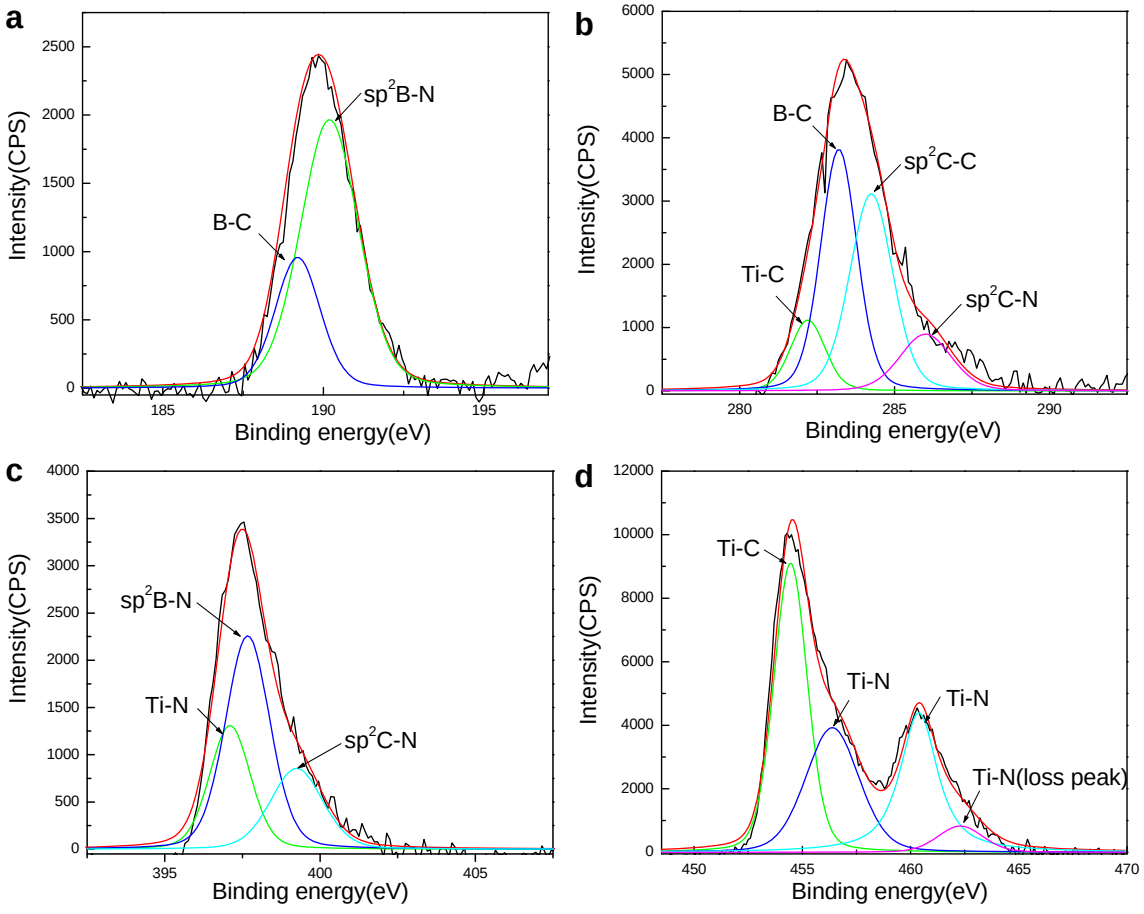

Fig. 2. XPS spectra of the as-deposited Ti–B–C–N coatings with 28.9 at.% C: (a) B 1s (b) C 1s (c) N 1s, and (d) Ti 2p.

for 5 s to assure that the indenter depth did not exceed 10% of the coating thickness (2–3 μm). Each hardness measurement was repeated 5 times to obtain the average.

3. Results and discussion

The elemental composition of the as-deposited Ti–B–C–N coatings derived from XPS is shown in Table 1. As carbon target power increase from 0 kW to 3 kW and 4 kW, the carbon contents increase from 28.9 at.% to 48.8 at.% and 54.2 at.%, while Ti, B, and N atom contents decrease gradually. The oxygen contents in range of 0.7–1.2 at.% can be detected in the coatings, which was most likely from residual oxygen in the deposition chamber.

The X-ray diffraction patterns of the as-deposited Ti–B–C–N coatings with different carbon contents in Fig. 1 show (111), (200), and (220) diffraction peaks of cubic Ti(C, N). As the carbon contents increase from 28.9 at.% to 48.8 at.% and 54.2 at.%, the peak intensity decreases but the peaks become broader. The average crystalline size calculated by Scherrer equation from broadening of diffraction peaks decrease from 24 nm to 8 nm and 6 nm with carbon content increase from 28.9 at.% to 48.8 at.% and 54.2 at.%. And as carbon content increase the lattice parameters of Ti(C, N) calculated from the (111), (200), and (220) diffraction peaks of Ti(C, N) increase from 0.426 nm to 0.428 nm, lattice parameters of the Ti(C, N) solid solution increase linearly with the increase of carbon concentration in Ti(C, N), reference to the lattice parameter data of Ti(C, N), we found that carbon content increase leads to the $TiC_{0.3}N_{0.7}$ phase gradually transforming to $TiC_{0.5}N_{0.5}$ phase [18,19].

Fig. 2 presents the B 1s, C 1s, N 1s, and Ti 2p core-level XPS spectra of the Ti–B–C–N coating with 28.9 at.% C. The B 1s spectrum in Fig. 2a can be fitted by two peaks, at 189.2 eV and 190.1 eV corresponding to B–C and B–N, respectively [20]. The C 1s spectrum in Fig. 2b can be fitted by four peaks at 282.1 eV, 283.2 eV, 284.6 eV, and 286.0 eV associated with Ti–C, B–C, sp^2C–C, and sp^2C–N, respectively [20–22]. The N 1s spectrum in Fig. 2c consists of three peaks centered at 397.0 eV, 397.8 eV, and 398.4 eV and the peaks arise from Ti–N, sp^2B–N, sp^3C–N, and sp^2C–N [20–22]. Fig. 2d shows that the Ti2p spectrum consists of spin doublets, and the two fitted peaks of Ti2p1/2 are at 454.6 eV and 455.8 eV corresponding to Ti–C and Ti–N, respectively. The Ti2p3/2 fitted peaks at 460.7 eV and 462.2 eV can be assigned to Ti–N and Ti–N loss peak, respectively [22]. As shown in the XRD spectrum, the nanocrystalline phase is composed of a Ti(C, N) solid solution, suggesting that the B–C, sp^2B–N, sp^2C–C, and sp^2C–N components exist in the amorphous phase and the Ti–B–C–N coatings comprise nc-Ti(C, N) nano-crystals embedded into an amorphous a-C/a-CN/a-BN/a-BC matrix. The reason for formation of the B–N, B–C, C–N, C–C bonds existed in amorphous by means of the thermodynamic driving force is not strong enough in reactive magnetron sputtering [21]. Some researchers also detected the Ti–B bonds in the Ti–B–C–N coatings, but in our samples the Ti–B bonds can't be detected, it may be caused by that in our samples the carbon

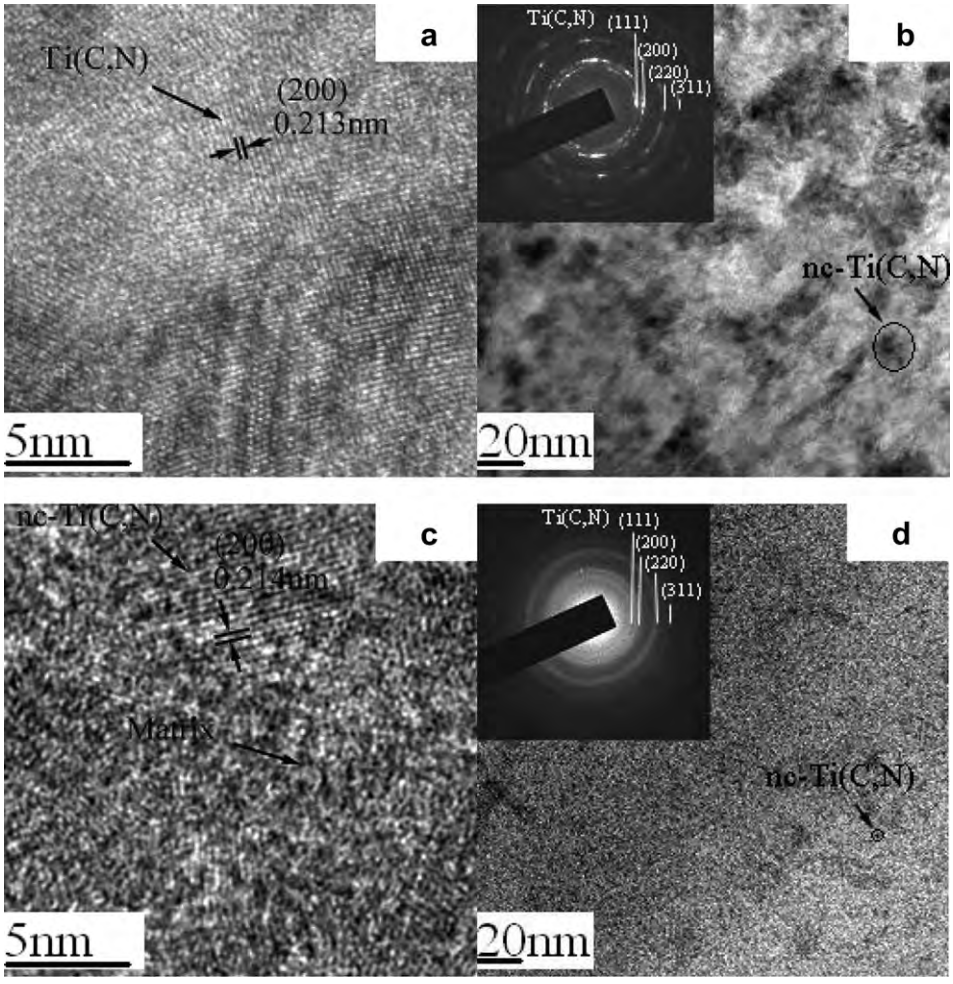

Fig. 3. HR-TEM images and SAD patterns of the as-deposited Ti–B–C–N coatings with carbon contents of: (a, b) 28.9 at.% and (c, d) 54.2 at.%.

content is higher than 28.9 at.%, while the B content is low, so it is easier to form Ti–C bonds than Ti–B bonds [12–14].

Fig. 3 shows the plan view HR-TEM images and selected area electron diffraction (SAD) patterns of the Ti–B–C–N coatings with carbon contents of (a, b) 28.9 at.% and (c, d) 54.2 at.%. In Fig. 3a, the {200} lattice fringes of Ti(C, N) with lattice spacing of 0.213 nm can be observed. The SAD patterns and the low magnification image in Fig. 3b confirm that the nano-crystallite is Ti(C, N), and the size of the nc-Ti(C, N) is about 20–30 nm. The {200} lattice fringes of Ti(C, N) with lattice spacing of 0.214 nm can be observed in the high magnification image of Fig. 3c. The low magnification image in Fig. 3d shows that the Ti(C, N) nano-crystallites size is about 3–7 nm. HR-TEM further confirms that the Ti–B–C–N coatings possess a nano-composite structure consisting of nc-Ti(C, N) embedded in the a-C/a-CN/a-BN/a-BC matrix and with increasing carbon concentration, the size of the nano-crystals decreases, the carbon concentration in nc-Ti(C, N) solid solution increase.

The XRD patterns of the Ti–B–C–N coatings after oxidation at elevated temperature are presented in Fig. 4 to provide information about the microstructural evolution. The intensity of the (111) and (200) peaks of Ti(C, N) decreases with oxidation temperature, and Ti_3O_5 and TiO_2 phases can be identified from the coatings after oxidation. No oxide diffraction peaks can be detected until 800 °C from the 28.9 at.% C coating [Fig. 4a]. However, with regard to the coatings with carbon concentrations of 48.8 and 54.2 at.%, oxide diffraction peaks can be observed after annealing at 600 °C [Fig. 4b and c]. The XRD patterns indicate that addition of carbon reduces the oxidation resistance of the Ti–B–C–N system.

The HR-TEM images of the Ti–B–C–N coatings with 28.9 at.% C after annealing at 700 °C and 800 °C are depicted in Fig. 5. Fig. 5a and b reveal that after annealing at 700 °C, the coatings still possess a structure composed by nano-crystalline nc-Ti(C, N) embedded in an amorphous a-C/a-CN/a-BN/a-BC matrix, and the structure is similar to that of the as-deposited coatings. However, after annealing at 800 °C, the coating shows a mixed crystalline phase composed by nc-Ti(C, N) and nc-TiO_2 as revealed by the lattice fringes and SAD pattern in Fig. 5c and d which also indicates that TiO_2 is dominant. The micro-structure disclosed by HR-TEM confirms that the Ti–B–C–N coating with 28.9 at.% C can resist oxidation at 700 °C but not at 800 °C.

Fig. 6 shows that weight loss per unit surface area from the coatings as a function of annealing temperature. The Ti–B–C–N coating with 28.9 at.% C begins to lose weight at about 700 °C, whereas the Ti–B–C–N coatings with 48.8 and 54.2 at.% C begin to lose weight at about 600 °C. Oxidation can be divided into two stages: slow weight loss (Ti–B–C–N coating with 28.9 at.% C at 700 °C as well as Ti–B–C–N coatings with 48.8 and 54.2 at.% C at 600 °C) and fast weight loss (Ti–B–C–N coating with 28.9 at.% C at 800 °C and Ti–B–C–N coatings with 48.8 and 54.2 at.% C at 700 °C and 800 °C). The higher the carbon concentration, the more is the weight loss after annealing at 600–800 °C.

Fig. 7 shows the micro-hardness values of the three coatings as a function of annealing temperature. The micro-hardness of the Ti–B–C–N coating with 28.9 at.% C remains at about 15 GPa until 600 °C and after annealing at 700 °C, the micro-hardness decreases a little to 13 GPa. As the annealing temperature is further increased to 800 °C, the micro-hardness diminishes to about 7 GPa. In comparison, the micro-hardness values of the Ti–B–C–N coatings with 48.8 and 54.2 at.% C begin to decrease at 600 °C, and as annealing temperature is further increased to 700 °C and 800 °C, the micro-hardness values decrease obviously. The micro-hardness of the coating with 54.2 at.% C decreases more quickly than the coating with 48.8 at.% C.

Fig. 8 shows that the surface roughness of the coatings as a function of oxidation temperature. The surface roughness of the

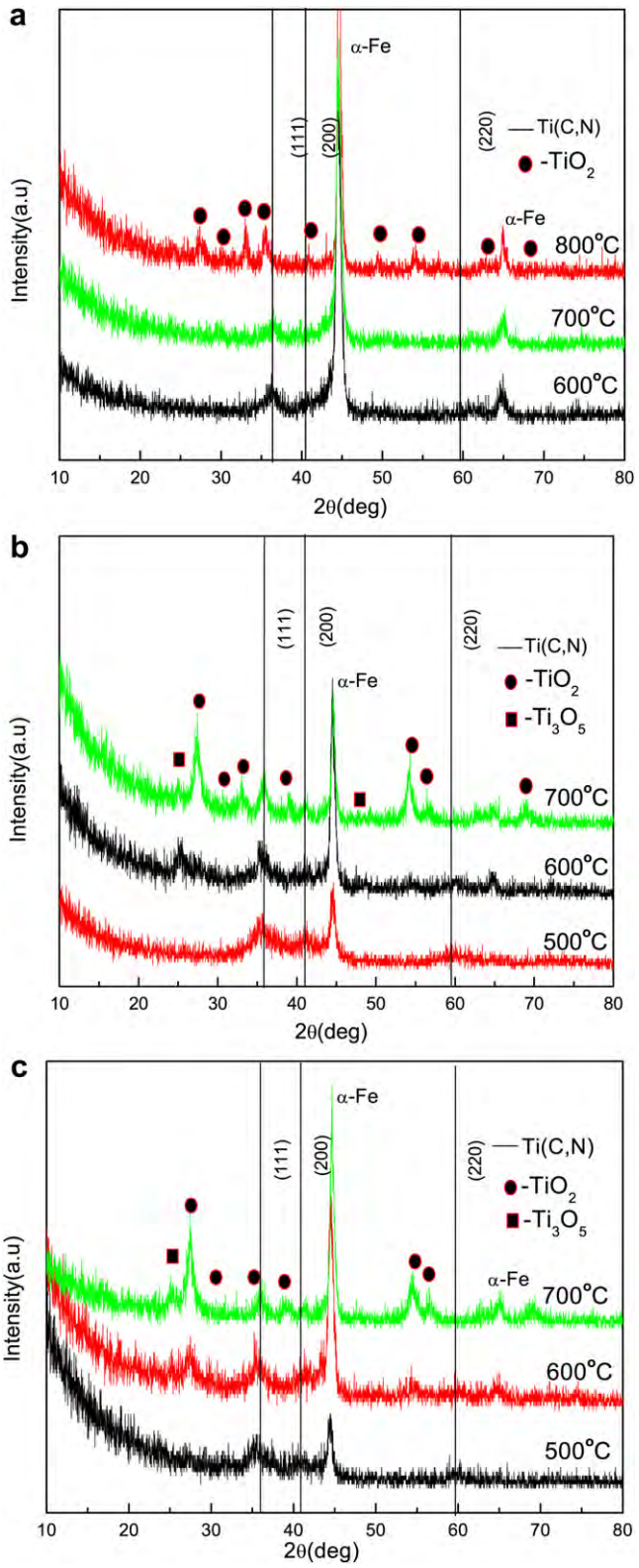

Fig. 4. X-ray diffraction patterns of the annealed Ti–B–C–N coatings with carbon contents of: (a) 28.9 at.%, (b) 48.8 at.%, and (c) 54.2 at.%.

Ti–B–C–N coating with 28.9 at.% C does not change much in the temperature range of 300 and 600 °C, but at 700 °C and 800 °C, the surface roughness increases monotonically to a maximum value of about 64 nm. In comparison, the surface roughness values of the Ti–B–C–N coatings with 48.8 and 54.2 at.% C increase to about

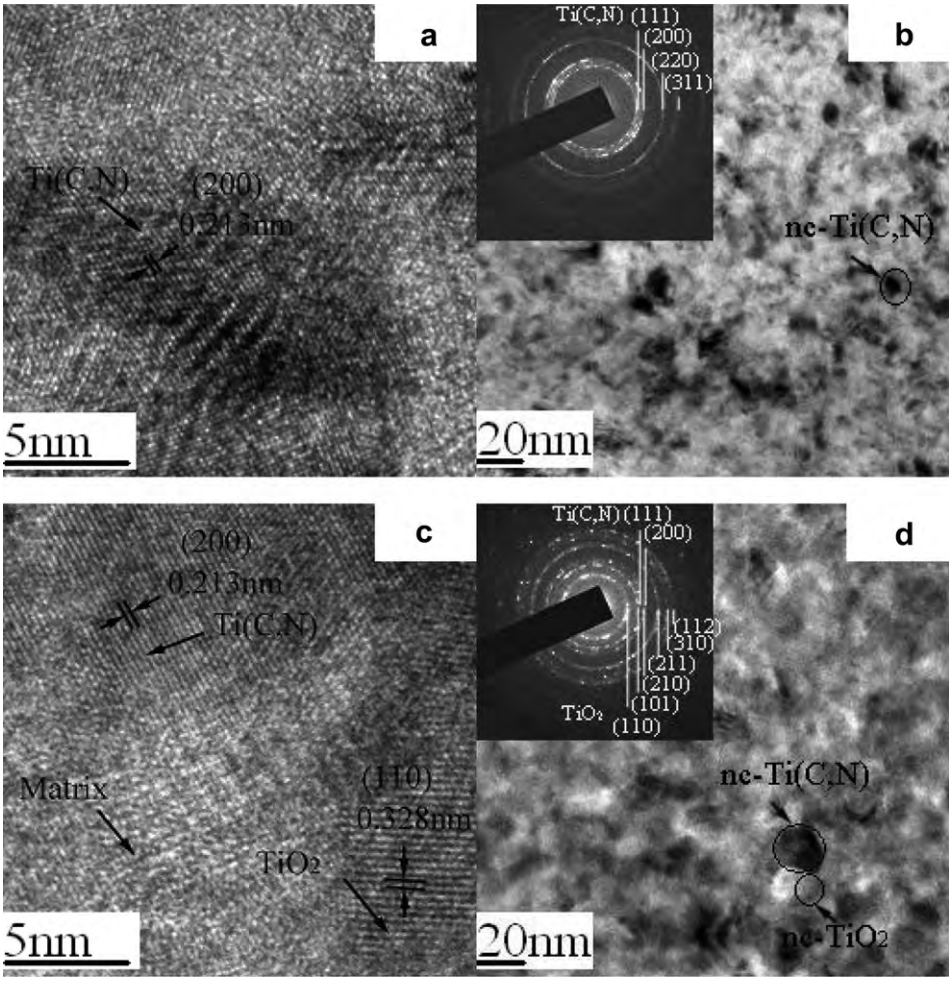

Fig. 5. HR-TEM images and SAD patterns of the Ti–B–C–N coatings with 28.9 at.% C after annealing at (a, b) 700 °C and (c, d) 800 °C.

40 nm after annealing at 600 °C. Fig. 8 also indicates that a higher carbon concentration translates into larger surface roughness after annealing at 600–800 °C. The evolution of the surface roughness is closely related to the micro-hardness and micro-structure change, confirming that the carbon concentration in the Ti–B–C–N coatings plays an important role in the oxidation resistance.

The change in the surface morphology of the Ti–B–C–N coating with 28.9 at.% C with annealing temperature observed by SEM is

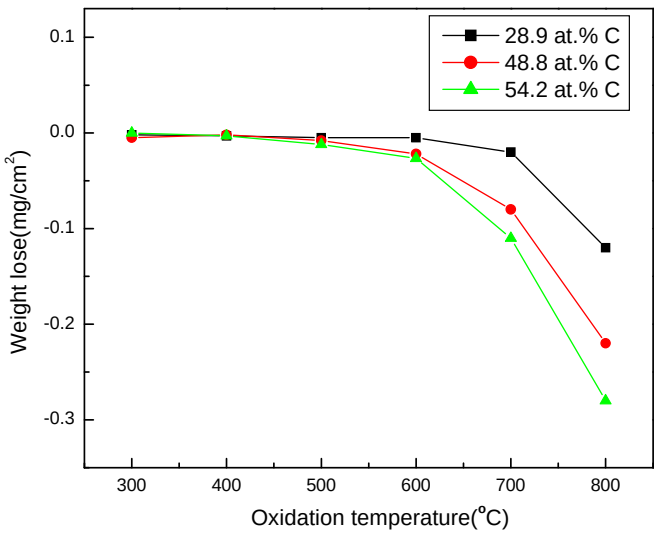

Fig. 6. Weight loss from the Ti–B–C–N coatings as a function of annealing temperature.

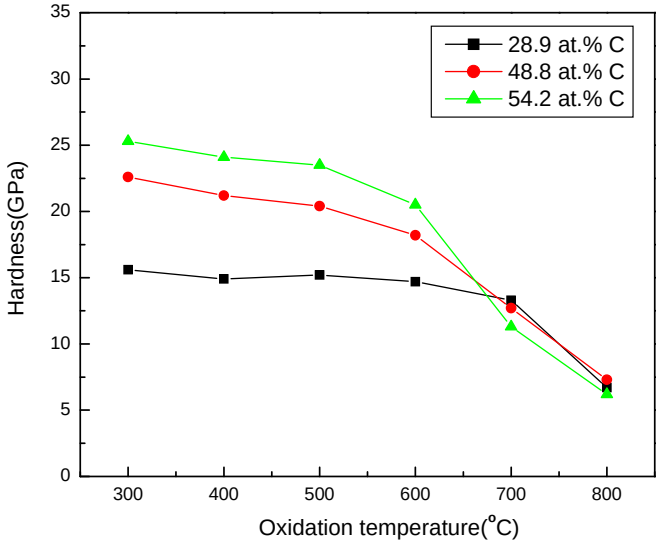

Fig. 7. Micro-hardness of the Ti–B–C–N coatings as a function of annealing temperature.

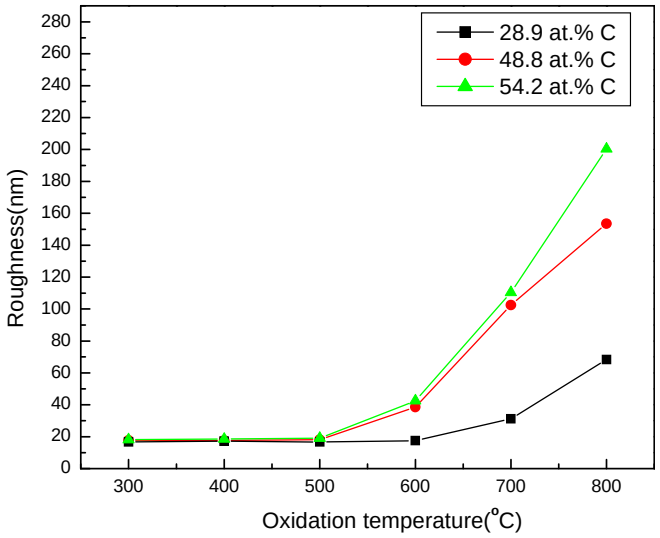

Fig. 8. Surface roughness of the Ti–B–C–N coatings as a function of annealing temperature.

presented in Fig. 9. The surface of the as-deposited coatings is smooth and particles with diameters of about 100–200 nm can be observed [Fig. 9a]. After annealing at 600 °C and 700 °C, the diameter of the particles increases and the boundaries between particles become clear. Some black pores can be observed from the boundary and some white-dots appear. This should be caused by internal stress produced during the heating and cooling process [Fig. 9b and c]. As the annealing temperature is increased to 800 °C, particles with diameters of about 100–200 nm disappear from the surface and the number and size of the black pores become larger, the white particles with sizes of about 20–30 nm can also be observed [Fig. 9d]. The HR-TEM and FE-SEM micro-analysis show that the distribution, size, composition, and micro-structure of these white particles is similar to nc-TiO_2 or nc-Ti_3O_5 crystallites transformed from the nc-Ti(C, N) as a result of oxidization [Figs. 5d and 9d].

The cross-sectional composition depth profiles of the Ti–B–C–N coatings with 28.9 at.% and 54.2 at.% carbon before and after oxidize at 800 °C measured by EDX are shown in Fig. 10. After oxidize at 800 °C the oxygen contents in both coatings increase obviously, the Fe contents increase a little, while the B, C, and N contents decrease. The composition depth profiles of the Ti–B–C–N coatings reveal that after oxidize at 800 °C the Ti–B–C–N coatings have been oxidized. Compare composition depth profiles of Ti–B–C–N coatings with 28.9 at.% and 54.2 at.% carbon, we found that the oxygen content in Ti–B–C–N coatings with 54.2 at.% carbon content is higher, which indicates that the oxidation of Ti–B–C–N coatings with 54.2 at.% carbon is more serious.

As aforementioned, the Ti–B–C–N coatings have a structure consisting of nano-crystalline nc-Ti(C, N) embedded in an amorphous a-C/a-CN/a-BN/a-BC matrix and carbon has an important effect on the micro-structure and oxidation behavior of the coatings. As the carbon content is increased from 28.9 to 54.2 at.%, the size of the nano-crystallites diminishes from 24 nm to 6 nm, and the on-set temperature of observable oxidation decreases from about 700 °C to 600 °C. The oxidation resistance study done by Lu YH on Ti–B–N coatings shows that low oxidation rate accompanied in Ti–B–N coatings with formation of small-grained Ti oxide occurred below 800 °C, while above 800 °C a rapid oxidation process accompanied with formation of large-grained Ti oxide with

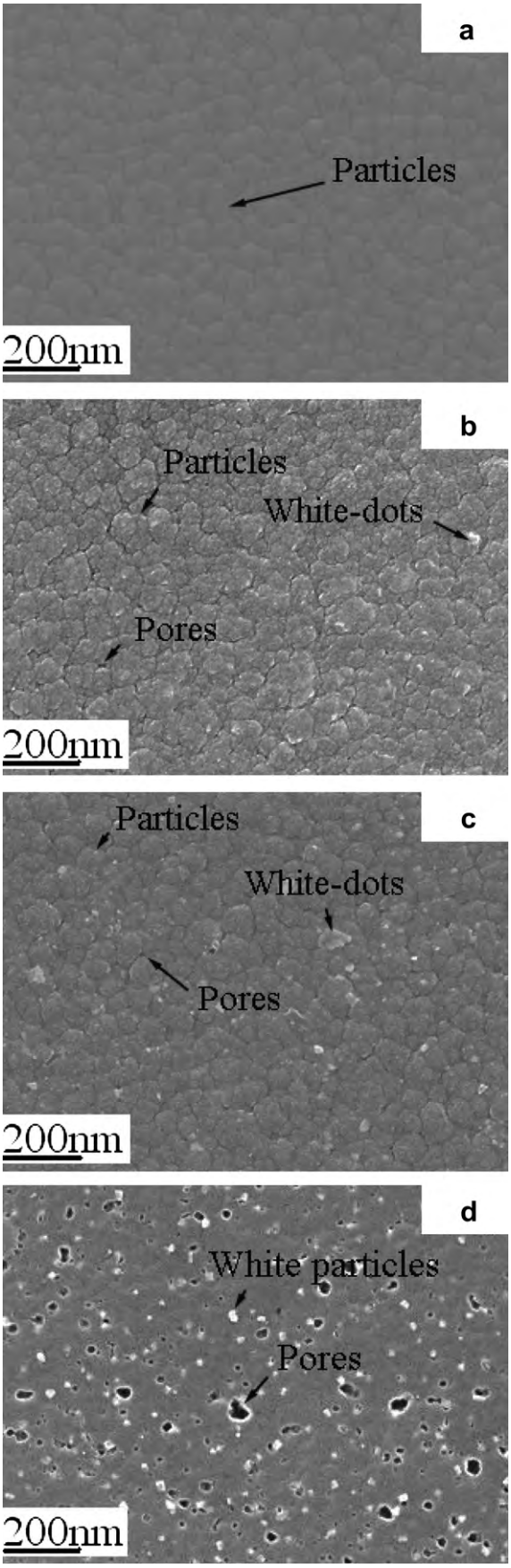

Fig. 9. SEM surface images of the Ti–B–C–N coatings with 28.9 at.% C: (a) as-deposited, (b) annealed at 600 °C, (c) annealed at 700 °C, and (d) annealed at 800 °C.

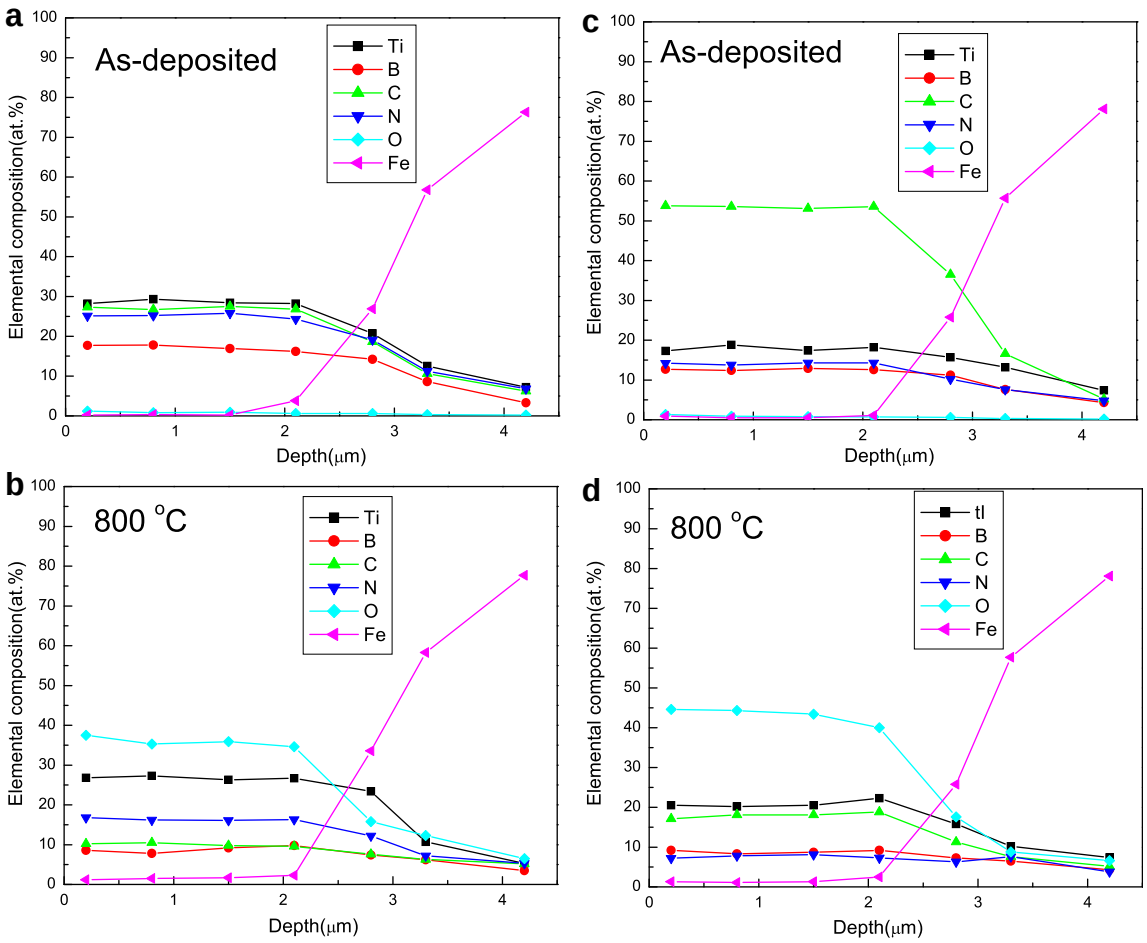

Fig. 10. Cross-sectional composition depth profiles of (a, b) 28.9 at.% C and (c, d) 54.2 at.% C Ti–B–C–N coatings before and after oxidized at 800 °C detected by EDX.

rough surface took place [1]. Compare oxidation behavior of the Ti–B–C–N coatings to Ti–B–N coatings we confirm that carbon content increase lead to the oxidation resistance of the coatings decrease. Following are main factors that impact the overall oxidation behavior.

The Ti–B–C–N coating with a smaller carbon concentration of 28.9 at.% has mainly the amorphous a-BN phase with very little free carbon or carbon nitride as shown in Fig. 2. It is because amorphous a-BN has good oxidation resistance at least below 800 °C. It can act as an efficient barrier against oxygen diffusion and protect the nc-Ti(C, N) phase from oxidation [1,23,24]. Hence, the coating cannot be easily oxidized below 700 °C. However, at 800 °C, the amorphous a-BN phase begins to react with the oxygen in air producing B_2O_3 as shown. The B_2O_3 can easily evaporate from the Ti–B–C–N surface during annealing leaving behind the defects such as pores, micro-cracks, and grain boundaries [1]. The defects can act as the high diffusivity paths for oxygen, which accelerated the formation and transportation of TiO_2 and Ti_3O_5 scales [1,16]. Besides this, Zhong D suggests that the diffusion and oxidation of Fe and N at elevated temperature can produce more oxygen vacancies, the oxygen vacancies are the mobile species in n-type semi-conducter TiO_2, and can accelerate oxidation of titanium [16].

Ti–B–C–N coatings with bigger carbon contents of 48.8 and 54.2 at.% C have higher concentration of the amorphous a-C/a-CN phase than that in the coating with 28.9 at.% C. Amorphous carbon usually has poor oxidation resistant properties and begins to react with oxygen at about 600 °C [25]. Hence, a-C/a-CN can be oxidized to CO and evaporation lead to the formation of defects which speed up oxidation when the temperature is 700 °C of higher.

4. Conclusion

Ti–B–C–N coatings fabricated by reactive magnetron sputtering have a nano-composite structure composed of nc-Ti(C, N) nanocrystals embedded in an amorphous a-C/a-CN/a-BN/a-BC matrix. The Ti–B–C–N coatings with carbon content of 28.9 at.% are stable at temperature below 700 °C. However, if the carbon concentration is increased to 48.8 and 54.2 at.%, the coatings begin to oxidize at 600 °C. The Ti(C, N) nano-crystallines in the coatings are gradually oxidized to TiO_2 or Ti_3O_5 as the oxidize temperature increase to 600 °C or higher, and carbon addition lead to the oxidation rates increase. The oxidation rates of the coatings and the Ti(C, N) nanocrystallines are controlled by oxygen diffusion, which is mainly affected by defect concentrations in the coatings.

Acknowledgements

This work was jointly supported by the International Science and Technology Cooperation Program of China (No.2008DFA51470), City University of Hong Kong Applied Research Grant (ARG) No. 9667038, and Hong Kong Research Grants Council (RGC) General Research Funds (GRF) No. CityU 112510.

References

[1] Lu YH, Shen YG, Zhou ZF, Li KY. J Vac Sci Technol A 2006;24:340.
[2] Mayrhofer PH, Stoiber M. Surf Coat Technol 2007;201:6148.
[3] Lu YH, Shen YG, Wang JP, Zhou ZF, Li KY. Surf Coat Technol 2007;201:7368.
[4] Wiedemann R, Weihnacht V, Oettel H. Surf Coat Technol 1999;116–119:302.
[5] Holzschuh H. Thin Solid Films 2004;469–470:92.
[6] Mollart TP, Haupt J, Gilmore R, Gissler W. Surf Coat Technol 1996;86-87:231.
[7] Lu YH, Shen YG, Zhou ZF, Li KY. Wear 2007;262:1372.
[8] Garcia-Luis A, Brizuela M, Onate JI, Sanchez-Lopez JC, Martinez-Martinez D, Lopez-Cartes C, et al. Surf Coat Technol 2005;200:734.
[9] Holzschuh H. Int J Refract Met Hard Mater 2002;20:143.
[10] Kim KH, Ok JT, Abraham S, Cho YR, Park IW, Moore JJ. Surf Coat Technol 2006; 201:4185.
[11] Shimada S, Takahashi M, Tsujino J, Yamazaki I, Tsuda K. Surf Coat Technol 2007;201:7194.
[12] Zhong D, Sutter E, Moore JJ, Mustoe GGW, Levashov EA, Disam J. Thin Solid Films 2001;398-399:320.
[13] Lin J, Mishra B, Moore JJ, Pinkas M, Sproul WD. Surf Coat Technol 2008; 203:588.
[14] Zhong D, Moore JJ, Mishra BM, Ohno T, Levashov EA, Disam J. Surf Coat Technol 2003;163:50.
[15] Vyas A, Lu YH, Shen YG. Surf Coat Technol 2010;204:1528.
[16] Chen X, Wang Z, Ma S, Ji V. Diamond Relat Mater 2010;19:1336.
[17] Uvarov V, Popov I. Mater Charact 2007;58:883.
[18] Zhang S. Mater Sci Eng A 1993;163:141.
[19] Cardinal S, Malchere A, Garnier V, Fantozzi G. Int J Refract Met Hard Mater 2009;27:521.
[20] Zhou ZF, Bello I, Lei MK, Li KY, Lee CS, Lee ST. Surf Coat Technol 2000;128-129:334.
[21] Ma S, Xu B, Wu G, Wang Y, Ma F, Ma D, et al. Surf Coat Technol 2008;202: 5379.
[22] Zhang G, Li B, Jiang B, Yan F, Chen D. Appl Surf Sci 2009;255:8788.
[23] Cofer CG, Economy J. Carbon 1995;33:389.
[24] Meng XL, Lun N, Qi YX, Zhu HL, Han FD, Yin LW, et al. J SolidState Chem 2011; 184:859.
[25] Luo X, Robin JC, Yu S. Nucl Eng Des 2004;227:273.